# Analysis of Multi-Layer Immiscible Fluid Flow in a Microchannel

**Jie Li**
Department of Mechanical and Aerospace Engineering,
NC State University,
Raleigh, NC 27695-7910

**Paul S. Sheeran**
Joint Departments of Biomedical Engineering,
UNC Chapel Hill and NC State University,
Chapel Hill, NC 27599

**Clement Kleinstreuer**[1]
Department of Mechanical and Aerospace Engineering,
NC State University,
Raleigh, NC 27695-7910;
Joint Departments of Biomedical Engineering,
UNC Chapel Hill and NC State University,
Chapel Hill, NC 27599
e-mail: ck@eos.ncsu.edu

*The development of microfluidics platforms in recent years has led to an increase in the number of applications involving the flow of multiple immiscible layers of viscous electrolyte fluids. In this study, numerical results as well as analytic equations for velocity and shear stress profiles were derived for N layers with known viscosities, assuming steady laminar flow in a microchannel driven by pressure and/or electro-static (Coulomb) forces. Numerical simulation results, using a commercial software package, match analytical results for fully-developed flow. Entrance flow effects with centered fluid-layer shrinking were studied as well. Specifically, cases with larger viscosities in the inner layers show a very good agreement with experimental correlations for the dimensionless entrance length as a function of inlet Reynolds number. However, significant deviations may occur for multilayer flows with smaller viscosities in the inner layers. A correlation was deduced for the two-layer electroosmotic flow and the pressure driven flow, both being more complex when compared with single-layer flows. The impact of using power-law fluids on resulting velocity profiles has also been explored and compared to Newtonian fluid flows. The present model readily allows for an exploration of the impact of design choices on velocity profiles, shear stress, and channel distribution in multilayer microchannel flows as a function of layered viscosity distribution and type of driving force.* [DOI: 10.1115/1.4005134]

*Keywords: immiscible fluids, multilayer viscosities, non-newtonian fluids, pressure-driven flow, electroosmotic flow, microchannel entrance effects*

## 1 Introduction

The number of microfluidic applications involving the interaction of multiple immiscible fluid layers has grown dramatically in the last decade, as researchers established the usefulness of microfluidic platforms to solve a variety of science and engineering problems. Such microfluidic platforms involving precise control of complex fluid flow fields have become increasingly prevalent in micro-scale biomedical processing, emulsification, therapeutics, and lab-on-a-chip processes. Such applications fall into the categories of particle formation, e.g., droplets [1–4], bubbles [5], multilayer gas-core lipospheres [6], and "Jams" particles [7], as well as improved interface, diffusion and reaction phenomena [8–14], rheological measurements [8], and cell sorting and treatment [15–17].

Traditionally, fluid flow is accomplished via applied pressure gradients (e.g., Poiseuille flow) or translation/rotation of system geometries (e.g., Couette flow). For microchannel flow at low Reynolds numbers and without the need for mechanical (i.e., moving) parts, electroosmotic flow is a preferred alternative to pressure-driven flow (see Chapter 7 in Kleinstreuer [18]; among other texts). Briefly, in electroosmotic flow an external electric field is applied across a charged microchannel containing an ionized fluid. The induced electric potential decays exponentially from the wall for single-plate systems or in relatively wide channels. It acts measurably in the resulting electric double-layer (EDL), shown in Fig. 1. The EDL is composed of the Stern layer (immobile counter ions at the wall surface), and the moving "diffuse layer" of thickness $\lambda_D$, also known as the Debye length. Approximately within a nano-scale wall layer of $0 < y < 3\lambda_D$ the fluid flows in the direction of the applied electric field. The viscous resistance between layers of the fluid drags the bulk fluid outside the EDL in the same direction, creating a uniform velocity for the bulk fluid. In fact, for condition of, say, $3\lambda_D \ll \alpha H$ (see Figs. 1–3) it can be assumed that the electroosmotic velocity $u_{EO} = u_{bulk} \approx u_{slip}$ [19].

When immiscible fluid streams come into contact at the inlet section of a microchannel, the ultimate flow regime depends on the device geometry, flow rates, and instabilities that occur at the fluid-fluid interfaces. These layers have different viscosities, densities, and electrical properties, which will affect the velocity and shear-stress profiles significantly and allow for unique applications. For example, Gao et al. [20,21] obtained analytical solutions for velocity profiles and flow rates of two-liquid flow in a microchannel which was driven both by electroosmotic force and pressure gradient. Li et al. [22] analyzed the time-dependent, electroosmotic/pressure-driven flow of three immiscible fluids in a rectangular microchannel. However, in some applications; for example when employing the flow-focusing effect, it is important to consider more than three fluid layers, i.e., any number of layers subject to varying driving forces. For example, in Ward et al. [15] droplets were formed by three parallel flows converging at a geometrical narrowing. More recently, Hettiarachchi et al. [6] generated complex chemotherapeutic-loadable contrast agents for medical ultrasonography using five converging fluid layers. Theoretical evaluations towards design choices for such systems can be either numerical or analytical.

Elaborate numerical simulations may be performed to compare changes in geometry towards achieving a desired outcome; however, they are typically quite complex and often do not provide a basic understanding of transport phenomena in multilayer flows. Using basic geometries and simplifying assumptions, analytic solutions can be obtained with more traditional mathematics software. Thus, the present study provides a compact, theoretical model of steady laminar multilayer fluid flow. For applicability to

[1]Corresponding Author.

Contributed by the Fluids Engineering Division of ASME for publication in the JOURNAL OF FLUIDS ENGINEERING. Manuscript received June 30, 2011; final manuscript received September 16, 2011; published online xx xx, xxxx. Assoc. Editor: Prof. Ali Beskok.

  

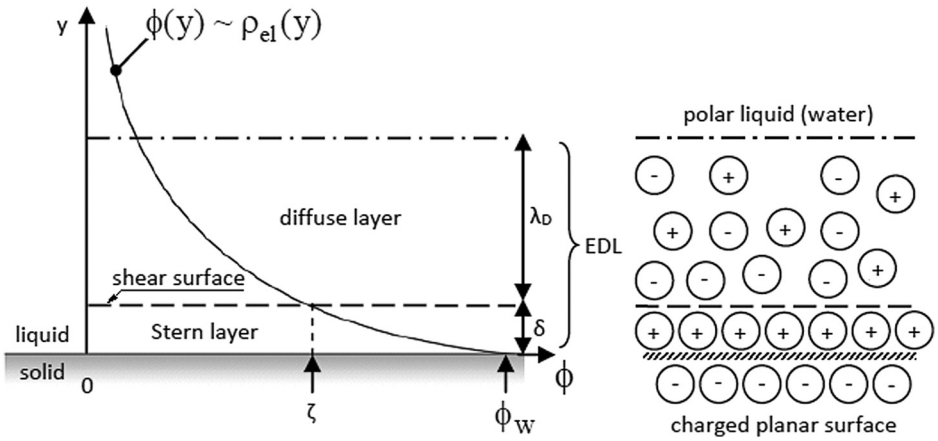


**Fig. 1 Profile of the electric potential $\phi(y)$ in an electric double layer (EDL)**

a wide variety of platforms, the model has been evaluated considering different driving forces, i.e., electroosmotic and/or pressure forces. Two important design considerations have to be taken into account, i.e., immiscible layers must operate under low Reynolds numbers to preserve interface stability [14] and Joule heating should be avoided to remain below critical system temperatures. It should be noted that in some cases interface instability is a desired outcome to create droplets based on surface tension effects [17].

In this paper, an analytical solution has been developed for *N*-layers of pressure-driven, electroosmotic as well as combined pressure/electroosmotic flows, assuming steady fully-developed immiscible fluid layers in rectangular microchannels. The programmable analytic model is most convenient for the exploration of viscous effects in the different layers as well as for the exploration of layer-height effects. In addition, entrance effects, dominant in microfluidic systems, with viscous layer development as well as power-law fluids were simulated numerically. This model is of use when analyzing fluid properties and system parameters of multiple-layer interactions as they relate to more complex industrial applications.

## 2 Theory

**2.1 Governing Equations.** The continuum mechanics equations describing the transport phenomena are based on the following assumptions:

- The fluid flow is incompressible, steady, and laminar
- The no-slip boundary condition holds
- Planar interfaces between the immiscible fluids prevail
- Layer-interface matching conditions are equal velocities and shear stresses
- Gravity does not affect (horizontal) microchannel flow

Thus, the reduced and modified Cauchy equations read [18,23,24]:

$$\nabla \cdot \vec{\mathbf{v}} = 0 \tag{1}$$

$$\rho(\vec{\mathbf{v}} \cdot \nabla)\vec{\mathbf{v}} = -\nabla p + \nabla \cdot \vec{\tau} + \vec{\mathbf{f}}_{\mathrm{el}} \tag{2}$$

where

$$\vec{\tau} = \begin{cases} \mu \nabla \vec{\mathbf{v}} & \text{for Newtonian fluids} \\ \eta \nabla \vec{\mathbf{v}} & \text{for power} - \text{law fluids} \end{cases} \tag{3a,b}$$

and $\vec{\mathbf{f}}_{\mathrm{el}}$ is the Coulomb electric force per unit volume acting inside the electric double layer (EDL), $\rho_{el}$ is the charge density, $\varepsilon$ is the dielectric constant, $\vec{\mathbf{E}}$ is the external electric field applied, and $\phi$ is the electric potential (see Fig. 1). Specifically,

$$\vec{\mathbf{f}}_{\mathrm{el}} \equiv \rho_{el}\vec{\mathbf{E}} = -\varepsilon \vec{\mathbf{E}} \nabla^2 \phi \tag{3c}$$

While $\mu$ is a constant, $\eta$ is the apparent viscosity [18]:

$$\eta = m\dot{\gamma}^{n-1} \tag{4}$$

where the constants m and n characterize the fluid and $\dot{\gamma}$ is the shear rate. Clearly, when $n = 1$ and $m = \mu$ a Newtonian fluid is recovered, while $n < 1$ represents a pseudoplastic fluid or shear-thinning fluid and $n > 1$ a dilatant fluid or shear-thickening fluid.

**2.2 Numerical Method.** Ansys CFX-12 software (ANSYS, Inc., Canonsburg, PA) was employed to analyze microchannel-entrance effects as well as multilayer flow characteristics, especially for power-law fluid flow, where the electroosmotic velocity

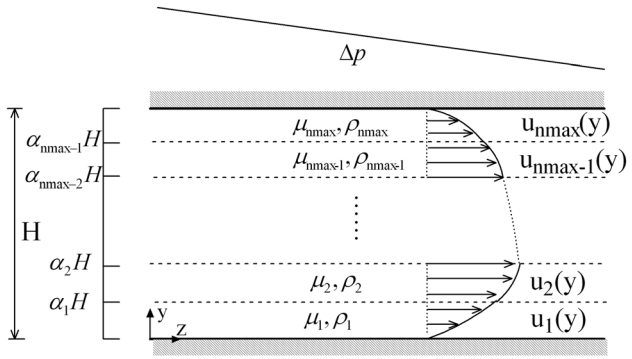


**Fig. 2 N-layer immiscible fluid Poiseuille-type flow**

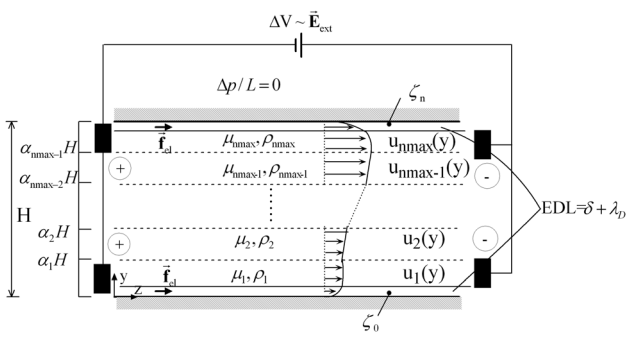


**Fig. 3 Idealized n-layer electro-osmotic flow in a microchannel with zero pressure gradient and electric double layer (EDL)**

($u_{EO}$) was employed as a $u_{slip}$-boundary condition to capture the electroosmotic flow effect. The computations were performed on an IBM Linux Cluster at North Carolina State University's High Performance Computing Center (Raleigh, NC) and on a local dual Xeon Intel 3.2G Dell desktop (C M-P Laboratory, MAE Department, NC State University). Mesh independence was examined and verified by increasing the nodal number by 50% which produced a maximum result change of just 0.85% for the velocity field. The unstructured mesh for a typical case contained 334080 hexahedral elements with 367710 nodes for fluid domain. Furthermore, the solutions of the flow field were assumed to be converged when the dimensionless mass and momentum residual ratios were below $10^{-6}$. Improving the convergence criteria to less than $10^{-7}$ had a negligible effect on the simulation results. A typical simulation run took about 12 hs.

To investigate multilayer fluid flow, the microchannel Reynolds number is defined as the sum of sub-Reynolds numbers of each layer, where the sub-Reynolds number is determined by its own hydraulic diameter and viscosity. Thus,

$$\mathrm{Re} = \sum_{i=1}^{n} \mathrm{Re}_i \tag{5}$$

and

$$\mathrm{Re}_i = \frac{\rho U D_{h_i}}{\mu_i} \tag{6}$$

where $D_{hi} = (4S_i/P_i)$ is the i-layer hydraulic diameter and U is the average velocity at the channel inlet. For example, when there are three layers of the same fluid in a microchannel of height H, the combined Reynolds number is identical to single-layer channel flow, i.e., $\mathrm{Re} = \mathrm{Re}_1 + \mathrm{Re}_2 + \mathrm{Re}_3 = (\rho U(1/3)2H/\mu) \times 3 = (\rho U 2H/\mu)$.

Entrance effects may be very important for flow in microfluidic devices. Atkinson et al. [25] and Chen [26] provided correlations for the entrance length of parallel-plate flow of a single layer as:

$$\frac{Le}{D_h} = 0.3125 + 0.011\mathrm{Re} \tag{7}$$

and

$$\frac{Le}{D_h} = \frac{0.315}{0.0175\mathrm{Re} + 1} + 0.011\mathrm{Re} \tag{8}$$

The correlation of Chen [26] (i.e., Eq. (8)) may be more accurate for low Reynolds numbers, say, Re = 0.5 to 5.

## 2.3 Analytical Results

*2.3.1 N-Layer Poiseuille Flow.* Fig. 2 provides the schematics of N-layer Poiseuille-type immiscible fluid flow in a microchannel, where each layer ends at a height specified by the coefficient $\alpha_i$. For example, height $\alpha_1 H$ specifies the bottom boundary of layer one. The following rule applies to the height coefficients (where layer $\mathrm{N_{max}}$ ends at the solid boundary interface):

$$0 < \alpha_1 < \alpha_2 < \cdots < \alpha_{\mathrm{Nmax}-1} < 1 \tag{9}$$

For 2D flow with a constant pressure gradient, Eq. (2) can be reduced to:

$$\frac{d^2u}{dy^2} = -\frac{\Delta p}{\mu L} \tag{10}$$

while the shear stress is:

$$\tau_{zy} = \mu \frac{du}{dy} \tag{11}$$

Applying this to $n$-layers of immiscible fluid flow (see Fig. 2), the following boundary conditions arise.

At solid surfaces:

$$u_1(y = 0) = 0 \tag{12a}$$

and

$$u_{\mathrm{Nmax}}(y = H) = 0 \tag{12b}$$

at liquid-liquid interfaces ($n > 1$):

$$u_i(y = \alpha_i H) = u_{i+1}(y = \alpha_i H); \quad 1 \le i \le \mathrm{N_{max}} - 1 \tag{13}$$

$$\tau_{zy,i}(y = \alpha_i H) = \tau_{zy,i+1}(y = \alpha_i H); \quad 1 \le i \le \mathrm{N_{max}} - 1 \tag{14}$$

With this generalized approach, Eq. (10) and Eq. (11) can be solved in terms of the i$^{\mathrm{th}}$-layer ($1 \le i \le \mathrm{N_{max}}$) and featuring coefficients $C_{i,1}$ and $C_{i,2}$ as:

$$u_i = -\frac{\Delta p}{2\mu_i L} y^2 + C_{i,1} y + C_{i,2} \tag{15}$$

and

$$\tau_{zy,i} = -\frac{\Delta p}{L} y + \mu_i C_{i,1} \tag{16}$$

Evaluating these coefficients in matrix form, the following relationships can be derived for Poiseuille-type flow

(1) All coefficients $\mathrm{C_i}$ have a common term dependent on $\mathrm{N_{max}}$, defined here as:

$$N_{COEF} = \frac{\sum_{j=1}^{\mathrm{Nmax}-1} \alpha_j \left[ \frac{\alpha_j(\mu_{j+1} - \mu_j)}{\mu_{\mathrm{j+1}}\mu_j} \prod_{i=1}^{\mathrm{Nmax}} \mu_{\mathrm{i}} \right] + \prod_{j=1}^{\mathrm{Nmax}-1} \mu_{\mathrm{j}}}{\sum_{j=1}^{\mathrm{Nmax}-1} \left[ \frac{\alpha_j(\mu_{j+1} - \mu_j)}{\mu_{\mathrm{j+1}}\mu_j} \prod_{i=1}^{\mathrm{Nmax}} \mu_{\mathrm{i}} \right] + \prod_{j=1}^{\mathrm{Nmax}-1} \mu_{\mathrm{j}}} \tag{17}$$

(2) The $C_{i,1}$ coefficient is given as:

$$C_{i,1} = \frac{\Delta p}{2\mu_i L} H N_{COEF} \tag{18}$$

(3) The $C_{i,2}$ coefficient reads:

$$C_{i,2} = \frac{\Delta p}{2L} H^2 \sum_{j=1}^{\mathrm{i}-1} \left[ \alpha_j \frac{(N_{COEF} - \alpha_j)(\mu_{j+1} - \mu_j)}{\mu_{j+1}\mu_j} \right] \tag{19}$$

Hence, the generalized solution for the velocity profile of each layer can be expressed as:

$$u_i = \frac{\Delta p H^2}{2\mu_i L} \left\{ -\left(\frac{y}{H}\right)^2 + \frac{N_{COEF} y}{H} + \mu_i \sum_{j=1}^{\mathrm{i}-1} \left[ \alpha_j \frac{(N_{COEF} - \alpha_j)(\mu_{j+1} - \mu_j)}{\mu_{j+1}\mu_j} \right] \right\} \tag{20}$$

The generalized solution for the shear stress at each layer-interface is:

$$\tau_{zy,i} = \frac{\Delta p H}{L} \left( -\frac{y}{H} + \frac{N_{COEF}}{2} \right) \tag{21}$$

*2.3.2 N-layer Electroosmotic Flow.* For electroosmotic flow a new body force per unit volume, $\vec{\mathbf{f}}_{\mathrm{el}}$, inside the diffuse layer of thickness $\lambda_D$ (see Fig. 1 and Eq. (2)), has to be considered. Figure 3 depicts the schematics of *N*-layer electroosmotic flow in a microchannel with zero pressure gradient and EDL. The immiscible, *N*-layer fluids may include some conducting liquids and nonconducting liquids. We assumed that only two conducting fluids are in the microchannel, i.e., the bottom layer and the top layer, i.e., the $\zeta$ potential at the fluid-fluid interface does not only depend on the wall potential and the ionic properties of the two liquids, but also on the *p*H-values and the concentration of the electrolyte [27,28]. Thus, the fluid-fluid interfacial $\zeta$ potential is set to zero for the analytical solution. Depending on the effective electroosmotic force, the fluid-layer velocities and hence the interface positions can be controlled. Specifically, the charge density $\rho_{el}$ along the wall is mainly confined to the EDL, following a Boltzmann distribution [23]. In the Debye-Hueckel limit we have:

$$\rho_{el}(y) = -\frac{\varepsilon}{\lambda_D^2}\phi \tag{22}$$

so that $\nabla^2\phi$ in Eq. (3*b*) can be replaced, i.e.,

$$\nabla^2\phi = \frac{\phi}{\lambda_D^2} \tag{23}$$

Equation (23) can be approximately solved by applying the following boundary conditions in the thin layers near the walls, which are based on the present assumption that $3\lambda_D \ll \alpha H$ [24]:

$$\phi_w = \begin{cases} \phi(y=0) \approx \zeta_1 \\ \phi(y=H) \approx \zeta_{\mathrm{Nmax}} \end{cases} \tag{24a}$$

$$\phi = \begin{cases} \phi(y \approx 3\lambda_D) \\ \phi(y \approx H - 3\lambda_D) \end{cases} \approx 0 \tag{24b}$$

Clearly, assuming the typical exponential decay of $\phi(y)$, at $y \approx 3\lambda_D$, $\phi \approx 0.05\zeta$. Solving Eq. (23) subject to Eqs. (24*a*) and (24*b*) and noting $\phi(3\lambda_D \le y \le H - 3\lambda_D) = 0$, we have:

$$\phi = \begin{cases} -\dfrac{\cosh(3)}{\sinh(3)}\zeta_1 \sinh(y/\lambda_D) + \zeta_1 \cosh(y/\lambda_D) & 0 \le y \le 3\lambda_D \\ 0 & 3\lambda_D \le y \le H - 3\lambda_D \\ \dfrac{\cosh(3)}{\sinh(3)}\zeta_{\mathrm{Nmax}} \sinh[(y - H + 3\lambda_D)/\lambda_D] - \zeta_{\mathrm{Nmax}} \cosh[(y - H + 3\lambda_D)/\lambda_D] + \zeta_{\mathrm{Nmax}} & H - 3\lambda_D \le y \le H \end{cases} \tag{25}$$

So, a reduced form of Eq. (2) in conjunction with Eq. (3*a*) now reads:

$$\mu_i \frac{d^2 u_i}{dy^2} + \mathrm{f}_{\mathrm{z}}^{el} = 0 \tag{26}$$

and with Eq. (3*b*) we have:

$$\frac{d^2}{dy^2}\left[u_i(y) - \frac{\varepsilon E_0}{\mu_i}\phi(y)\right] = 0 \tag{27}$$

subject to the following boundary conditions.

At the walls:

$$u_1(y=0) = 0 \tag{28a}$$

$$u_{\mathrm{Nmax}}(y=H) = 0 \tag{28b}$$

and at the interfaces ($n > 1$):

$$u_i(y = \alpha_i H) = u_{i+1}(y = \alpha_i H); \quad 1 \le i \le \mathrm{N_{max}} - 1 \tag{29a}$$

$$\tau_{zy,i}(y = \alpha_i H) = \tau_{zy,i+1}(y = \alpha_i H); \quad 1 \le i \le \mathrm{N_{max}} - 1 \tag{29b}$$

Taking this generalized approach, the solutions for the $\mathrm{i^{th}}$-layer ($1 \le i \le \mathrm{N_{max}}$) with coefficients $D_{i,1}$ and $D_{i,2}$ are:

$$u_i - \frac{\varepsilon E_0}{\mu_i}\phi(y) = D_{i,1}y + D_{i,2} \tag{30}$$

and

$$\tau_{zy,i} = \varepsilon E_0 \frac{d\phi}{dy}\bigg|_{y=\alpha_i H} + \mu_i D_{i,1} \tag{31}$$

Again, evaluating these coefficients in matrix form, the following relationships can be derived for the electroosmotic flow.

(1) All coefficients $\mathrm{D_i}$ have a common term dependent on $\mathrm{N_{max}}$, defined here as:

$$M_{COEF} = \frac{\left[\dfrac{\zeta_{\mathrm{Nmax}}}{\mu_{\mathrm{Nmax}}} - \dfrac{\zeta_1}{\mu_1}\right]}{\displaystyle\sum_{j=1}^{\mathrm{Nmax}-1}\left[\alpha_j\left(\frac{\mu_1}{\mu_j} - \frac{\mu_1}{\mu_{j+1}}\right)\right] + \frac{\mu_1}{\mu_{\mathrm{Nmax}}}} \tag{32}$$

(2) The $D_{i,1}$ coefficient is given as:

$$D_{i,1} = \frac{\varepsilon E_0}{H}\frac{\mu_1}{\mu_i}M_{COEF} \tag{33}$$

(3) The $D_{i,2}$ coefficient reads:

$$D_{i,2} = \varepsilon E_0 M_{COEF}\sum_{j=1}^{i-1}\left[\alpha_j\left(\frac{\mu_1}{\mu_j} - \frac{\mu_1}{\mu_{j+1}}\right)\right] - \frac{\varepsilon E_0 \zeta_1}{\mu_1} \tag{34}$$

Finally, the generalized form of the velocity profile for each layer can be expressed as:

$$u_i = \frac{\varepsilon E_0}{H}\frac{\mu_1}{\mu_i}M_{COEF}y + \varepsilon E_0 M_{COEF}\sum_{j=1}^{\mathrm{i-1}}\left[\alpha_j\left(\frac{\mu_1}{\mu_j} - \frac{\mu_1}{\mu_{j+1}}\right)\right] - \frac{\varepsilon E_0 \zeta_1}{\mu_1} + \frac{\varepsilon E_0}{\mu_i}\phi(y) \tag{35}$$

The generalized form of the shear stress profile for each layer is:

$$\tau_{zy,i} = \frac{\varepsilon E_0}{H}\mu_1 M_{COEF} + \varepsilon E_0 \frac{d\phi}{dy} \tag{36}$$

*2.3.3 Combined Flow.* For combined electroosmotic and pressure-driven flow, we obtain the velocity profile by adding Eqs. (20) and (35):

$$u_i = \frac{\Delta p H^2}{2\mu_i L}\left\{-\left(\frac{y}{H}\right)^2 + \frac{N_{COEF}y}{H} + \mu_i \sum_{j=1}^{i-1}\left[\alpha_j \frac{(N_{COEF}-\alpha_j)(\mu_{j+1}-\mu_j)}{\mu_{j+1}\mu_j}\right]\right\} + \frac{\varepsilon E_0}{H}\frac{\mu_1}{\mu_i}M_{COEF}y + \varepsilon E_0 M_{COEF}\sum_{j=1}^{i-1}\left[\alpha_j\left(\frac{\mu_1}{\mu_j}-\frac{\mu_1}{\mu_{j+1}}\right)\right] - \frac{\varepsilon E_0 \zeta_1}{\mu_1} + \frac{\varepsilon E_0}{\mu_i}\phi(y) \tag{37}$$

*2.3.4 Flow Rate Comparisons.* For a 2D system with single layer (i.e., plate of width $W$ separated by $H$, where $W \gg H$), the electroosmotic and pressure-driven volumetric flow rates are:

$$Q_{PDF} = W\int_0^H \frac{\Delta p H^2}{2\mu L}\left\{-\left(\frac{y}{H}\right)^2 + \frac{y}{H}\right\}dy = \frac{\Delta p H^3 W}{12\mu L} \tag{38}$$

and

$$Q_{EOF} \approx W\int_0^H u_{EO}dy = -\frac{\varepsilon\xi_1}{\mu}E_0 HW = \mu_{EO}E_0 HW = \mu_{EO}(\Delta V/L)HW \tag{39}$$

Setting the net flow rate equal to zero [24] provides the necessary pressure drop over applied voltage as:

$$\frac{\Delta p}{\Delta V} = \frac{12\mu_{EO}\mu}{H^2} = -\frac{12\varepsilon\xi_1}{H^2} \tag{40}$$

Extension to multilayer flows yields:

$$Q = \sum_{i=1}^{\text{Nmax}-1} Q_i = \sum_{i=1}^{\text{Nmax}-1} W\int_{\alpha_{i-1}H}^{\alpha_i H} u_i dy \tag{41}$$

subject to $\alpha_{i-1} \le \frac{y}{H} \le \alpha_i$, $1 \le i \le N\text{max}$; $\alpha_0 = 0, \alpha_{N\,\text{max}} = 1$.

Inserting Eqs. (20) and (35) into Eq. (41) provides the flow rates for both multilayer pressure driven flow and electroosmotic flow. Employing a two-layer flow case for illustration, i.e., $\text{Nmax} = 2$, we have with Eqs. (17), (20), (32), (35), and (41):

$$Q_{PDF}^{2layer} = \frac{\Delta p H^3 W}{2\mu_1 L}\left[\left(\frac{4}{3}\frac{\mu_1}{\mu_2}-\frac{1}{3}\right)\alpha_1^3 + \left(\frac{1}{2}-\frac{3}{2}\frac{\mu_1}{\mu_2}\right)N_{COEF}\alpha_1^2 - \frac{\mu_1}{\mu_2}\alpha_1^2 + \frac{\mu_1}{\mu_2}N_{COEF}\alpha_1 + \frac{1}{2}\frac{\mu_1}{\mu_2}N_{COEF} - \frac{1}{3}\frac{\mu_1}{\mu_2}\right] \tag{42}$$

$$Q_{EOF} \approx \frac{W\varepsilon E_0 H}{\mu_1}\left[\frac{1}{2}M_{COEF}\mu_1\alpha_1^2\left(\frac{\mu_1}{\mu_2}-1\right) + M_{COEF}\mu_1\alpha_1\left(1-\frac{\mu_1}{\mu_2}\right) + \frac{1}{2}M_{COEF}\mu_1\frac{\mu_1}{\mu_2} - \xi_1\right] \tag{43}$$

Thus,

$$\frac{\Delta p}{\Delta V} = \frac{2\varepsilon}{H^2}\frac{\left[\frac{1}{2}M_{COEF}\mu_1\alpha_1^2\left(\frac{\mu_1}{\mu_2}-1\right) + M_{COEF}\mu_1\alpha_1\left(1-\frac{\mu_1}{\mu_2}\right) + \frac{1}{2}M_{COEF}\mu_1\frac{\mu_1}{\mu_2} - \xi_1\right]}{\left[\left(\frac{4}{3}\frac{\mu_1}{\mu_2}-\frac{1}{3}\right)\alpha_1^3 + \left(\frac{1}{2}-\frac{3}{2}\frac{\mu_1}{\mu_2}\right)N_{COEF}\alpha_1^2 - \frac{\mu_1}{\mu_2}\alpha_1^2 + \frac{\mu_1}{\mu_2}N_{COEF}\alpha_1 + \frac{1}{2}\frac{\mu_1}{\mu_2}N_{COEF} - \frac{1}{3}\frac{\mu_1}{\mu_2}\right]} \tag{44}$$

To test the results for single layer flow, i.e., $\mu_1 = \mu_2$, $\alpha_1 = 1.0$ and $\zeta_{\text{Nmax}} = \zeta_1$, we obtain $M_{COEF} = 0$ and $N_{COEF} = 1$. Substitution into Eq. (44) yields $(\Delta p/\Delta V) = -(12\varepsilon\xi_1/H^2)$, i.e., Eq. (40).

Based on dimensional analysis, the numerator of Eq. (44) is of the order of MAX(viscosity$^2$, $\zeta$ potential), i.e., typically $O(10^{-3})$. The denominator is of the order of one. Thus, Eq. (44) provides quantitative information when to use a micro-pump versus electroosmosis to obtain a desired flow rate in a microchannel.

*2.3.5 Height-Coefficient Analysis.* The interface and the height (or width) of a focused stream are important for sorting, separation, reaction and mixing in many applications [22,29]. Control of the interface allows for adjustment of the stream width. When applying the same flow rate in different layers, the variation of fluid viscosities and the magnitude and direction of the applied electric field can be used to adjust the stream width. For example, at the same volumetric flow rate, the more viscous fluid has to spread over a larger cross-sectional area; thus occupying a larger portion of the channel. The electroosmotic effect can further adjust the interface position, where the conducting fluid becomes "more viscous" or "less viscous" because the electric field changes the flow resistance at the flow interface.

For the present case, the cross-sectional area is simply described as $\text{A} = \text{W} \times \text{H}$, where W is the unit width. Now, to keep the same flow rate at each layer, the *height coefficients* should follow:

$$q_i = \int_{\alpha_{i-1}H}^{\alpha_i H} u_i dy = Q/\Delta W = q. \tag{45}$$

subject to $\alpha_{i-1} \le \frac{y}{H} \le \alpha_i$, $1 \le i \le \text{Nmax}$; $\alpha_0 = 0, \alpha_{\text{Nmax}} = 1$.

In summary, for any given flow rate the final layer distribution can be achieved according to the velocity profile in each layer.

## 3 Verification

To determine the validity of the developed equation for steady laminar fully-developed N-layer immiscible fluid flow, some tests have been performed.

(1) With $\text{N}_{\text{max}} = 1$ (i.e., just one layer), the equation should produce the standard Poiseuille flow for pressure-driven flow and the standard electroosmotic flow for electric force flow:
Using Eq. (17) and Eq. (32) with $\text{N}_{\text{max}} = 1$, the values of $N_{COEF}$ and $M_{COEF}$ are:

$$N_{COEF} = \frac{\sum_{j=1}^{0}\alpha_j\left[\frac{\alpha_j(\mu_{j+1}-\mu_j)}{\mu_{\text{j+1}}\mu_j}\prod_{i=1}^{1}\mu_{\text{i}}\right] + \prod_{j=1}^{0}\mu_{\text{j}}}{\sum_{j=1}^{0}\left[\frac{\alpha_j(\mu_{j+1}-\mu_j)}{\mu_{\text{j+1}}\mu_j}\prod_{i=1}^{1}\mu_{\text{i}}\right] + \prod_{j=1}^{0}\mu_{\text{j}}} = 1 \tag{46}$$

and

$$M_{COEF} = \frac{\left[\frac{\zeta_{\text{nmax}}}{\mu_1} - \frac{\zeta_0}{\mu_1}\right]}{\sum_{j=1}^{1}\left[\alpha_j\left(\frac{\mu_1}{\mu_j} - \frac{\mu_1}{\mu_{j+1}}\right)\right] + \frac{\mu_1}{\mu_1}} = \frac{\zeta_{\text{nmax}}}{\mu_1} - \frac{\zeta_0}{\mu_1} \quad (47)$$

As a result, for pure pressure-driven flow:

$$u_1 = \frac{\Delta p H^2}{2\mu_1 L}\left\{-\left(\frac{y}{H}\right)^2 + \frac{y}{H} + \mu_1 \sum_{j=1}^{0}\left[\alpha_j \frac{(1-\alpha_j)(\mu_{j+1}-\mu_j)}{\mu_{j+1}\mu_j}\right]\right\} \quad (48a)$$

and for pure electroosmotic flow with $\zeta_{\text{Nmax}} = \zeta_1$

$$u_1 = -\frac{\varepsilon E_0 \zeta_1}{\mu_1} + \frac{\varepsilon E_0}{\mu_1}\phi(y) \quad (48b)$$

Equations (48*a*) and (48*b*), reduce simply to:

$$u_1 = \frac{\Delta p H^2}{2\mu_1 L}\left\{-\left(\frac{y}{H}\right)^2 + \frac{y}{H}\right\} \quad (49a)$$

and

$$u_1 = \begin{cases} \frac{\varepsilon E_0 \zeta_1}{\mu_1} - \frac{\varepsilon E_0}{\mu_1}\left[-\frac{\cosh(3)}{\sinh(3)}\zeta_1 \sinh(y/\lambda_D) + \zeta_1 \cosh(y/\lambda_D)\right] & 0 \le y \le 3\lambda_D \\ \frac{\varepsilon E_0 \zeta_1}{\mu_1} & 3\lambda_D \le y \le H - 3\lambda_D \\ \frac{\varepsilon E_0 \zeta_1}{\mu_1} - \frac{\varepsilon E_0}{\mu_1}\left[\frac{\cosh(3)}{\sinh(3)}\zeta_1 \sinh[(y-H+3\lambda_D)/\lambda_D] - \zeta_1 \cosh[(y-H+3\lambda_D)/\lambda_D] + \zeta_1\right] & H - 3\lambda_D \le y \le H \end{cases} \quad (49b)$$

These velocity profiles match the Poiseuille expression for a single layer, horizontal parallel plate flow as well as the electroosmotic flow results.

Evaluating the shear-stress equations yields:

$$\tau_{zy} = \frac{\Delta p H}{L}\left(-\frac{y}{H} + \frac{1}{2}\right) \quad (50a)$$

and

$$\tau_{zy} = \varepsilon E_0 \frac{d\phi}{dy} \quad (50b)$$

As expected, the shear stress at the centerline (where y = 0.5 H) is zero.

(2) With $N_{\text{max}} = 2$ (i.e., two-layer), $\alpha_1 = 0.5$ and $\mu_1 = \mu_2$, the pressure driven flow should produce the standard Poiseuille profile for one layer (the same is true for any $N_{\text{max}}$ as long as each layer's viscosity is the same).

The $N_{COEF}$ value again results in $N_{COEF} = 1$ (due to the condition $\mu_1 = \mu_2$), which creates the following velocity profiles:

$$u_1 = \frac{\Delta p H^2}{2\mu_1 L}\left\{-\left(\frac{y}{H}\right)^2 + \frac{y}{H}\right\} \text{ subject to } 0 \le \frac{y}{H} \le 0.5 \quad (51a)$$

$$u_2 = \frac{\Delta p H^2}{2\mu_2 L}\left\{-\left(\frac{y}{H}\right)^2 + \frac{y}{H}\right\} \text{ subject to } 0.5 \le \frac{y}{H} \le 1.0 \quad (51b)$$

It is easy to see that with the same viscosities, the equations remain the same across the entire channel and can be condensed to:

$$u = \frac{\Delta p H^2}{2\mu L}\left\{-\left(\frac{y}{H}\right)^2 + \frac{y}{H}\right\} \text{ subject to } 0 \le \frac{y}{H} \le 1.0 \quad (52)$$

The shear stress profiles are obtained similarly, resulting in:

$$\tau_{zy} = \frac{\Delta p H}{L}\left(-\frac{y}{H} + \frac{1}{2}\right) \quad (53)$$

To test the interface position, we have

$$q_1 = \int_0^{\alpha_1 H} u_1 dy = \int_0^{\alpha_1 H} \frac{\Delta p H^2}{2\mu L}\left\{-\left(\frac{y}{H}\right)^2 + \frac{y}{H}\right\} dy = \int_{\alpha_1 H}^{H} \frac{\Delta p H^2}{2\mu L}\left\{-\left(\frac{y}{H}\right)^2 + \frac{y}{H}\right\} dy = q_2 \quad (54)$$

If the multilayer fluids flow at the same flow rate, the fluid of lower viscosity occupies less space. Solving Eq. (54), we can get $\alpha_1 = 0.5$.

(3) Considering pure electroosmotic flow with $N_{\text{max}} = 2$, $\alpha_1 = 0.5$, $\mu_1 = \mu_2$ and $\zeta_2 = \zeta_1$ the results are:

$$u_2 = -\frac{\varepsilon E_0 \zeta_1}{\mu_1} + \frac{\varepsilon E_0}{\mu_1}\phi(y) \text{ subject to } 0 \le \frac{y}{H} \le 0.5 \quad (55a)$$

and

$$u_2 = -\frac{\varepsilon E_0 \zeta_1}{\mu_1} + \frac{\varepsilon E_0}{\mu_2}\phi(y) \text{ subject to } 0.5 \le \frac{y}{H} \le 1.0 \quad (55b)$$

Equations (55*a*) and (55*b*), can combined to one equation describing the whole channel, i.e.,

$$u = -\frac{\varepsilon E_0 \zeta_1}{\mu} + \frac{\varepsilon E_0}{\mu}\phi(y) \text{ subject to } 0 \le \frac{y}{H} \le 1.0 \quad (56)$$

The shear stress profile can be obtained from Eqs. (25) and (36):

$$\tau_{zy,i} = -\varepsilon E_0 \frac{d\phi}{dy}$$
$$= \begin{cases} -\dfrac{\varepsilon E_0}{\lambda_D}\left[-\dfrac{\cosh(3)}{\sinh(3)}\zeta_1 \cosh(y/\lambda_D) + \zeta_1 \sinh(y/\lambda_D)\right] & 0 \le y \le 3\lambda_D \\ 0 & 3\lambda_D \le y \le H - 3\lambda_D \\ -\dfrac{\varepsilon E_0}{\lambda_D}\left[\dfrac{\cosh(3)}{\sinh(3)}\zeta_1 \cosh[(y-H+3\lambda_D)/\lambda_D] - \zeta_1 \sinh[(y-H+3\lambda_D)/\lambda_D]\right] & H - 3\lambda_D \le y \le H \end{cases} \quad (57)$$

(4) With $N_{max} = 1$, the combined electroosmotic and pressure-driven flow velocity profile can be derived from Eq. (37) with i = 1,$N_{COEF} = 1$ and $M_{COEF} = 0$ as:

$$u_1 = \frac{\Delta p H^2}{2\mu_1 L}\left\{-\left(\frac{y}{H}\right)^2 + \frac{y}{H}\right\} - \frac{\varepsilon E_0 \zeta_1}{\mu_1} + \frac{\varepsilon E_0}{\mu_1}\phi(y) \quad (58)$$

That same result can be obtained when solving:

$$0 = \frac{\partial p}{\partial x} + \mu\frac{\partial^2 u}{\partial y^2} + \rho_{el}E_0 \quad (59)$$

## 4 Results and Discussion

Equation (37) plus associated expressions are useful for analyzing numerous applications. For example, often up to five layers of immiscible fluids have to be controlled to create desired emulsion properties. To gain physical insight and demonstrate the model applicability, 2-, 3- and 4-layer flow profiles subject to different viscosity values and height coefficients for each layer have been simulated. Of interest is how flow fields interact over several layers, and how a layer's maximum velocity can be enhanced or reduced by adjusting the placement of layers as well as the height allotted to each layer. This insight can be especially useful for applications as those described by Wang et al. [16] and Takayama et al. [17], where careful design of laminar flows allows for spatial control of cell treatment and flow rates determining the treatment rate. First, the analytical results were compared with the numerical simulations to assure model accuracy and to gain basic physical insight. All equations were solved with the constant values listed in Table 1.

**4.1 Three-Layer Flow.** Figures 4–7 compare computer simulations with the theoretical results for pressure-driven flow, electroosmotic flow, and combined pressure/electroosmotic flow. As expected, all simulated profiles are in excellent agreement with the analytical results. Specifically, Fig. 4 shows the velocity profiles for an evenly-spaced, three-layer pressure-driven flow, where the velocities vary significantly due to changing fluid-layer viscosities. The maximum velocity was achieved by placing the most viscous fluid in the center, with the least viscous fluids along the walls. Clearly, in Case I the center-layer "rides" on the less viscous wall-layers in which the fluid flow swiftly "recovers" from the no-slip boundary condition. Case II represents the inverse scenario where the least viscous fluid occupies the center part of the channel. The two highly viscous wall layers resist fluid flow, drastically lowering the volumetric flow rate. When the fluid viscosity is decreased six-fold from top to bottom (see Case III), an asymmetric velocity profile is generated with the maximum velocity occurring in the bottom layer. The results shown in Fig. 4 also indicate that desired velocity profiles, and hence flow rates, can be

**Table 1 Parameter-values**

| Parameter | Value | Unit | Parameter | Value | Unit |
|---|---|---|---|---|---|
| $\Delta p$ | 1000 | Pa | $\varepsilon$ | $7.1 \times 10^{-10}$ | $C/Vm$ |
| $\mu$ | $0.9 \times 10^{-3}$ | $\frac{kg}{ms}$ | $D_h$ | 144 | $\mu m$ |
| $\rho$ | 1000 | $kg/m^3$ | L | 18 | mm |
| $E_0$ | 60000 | V/m | H | 72 | $\mu m$ |
| $\zeta_1$ | −24.4 | mV | $\lambda_D$ | 20 | nm |
| $\zeta_{Nmax}$ | −48.8 | mV | | | |

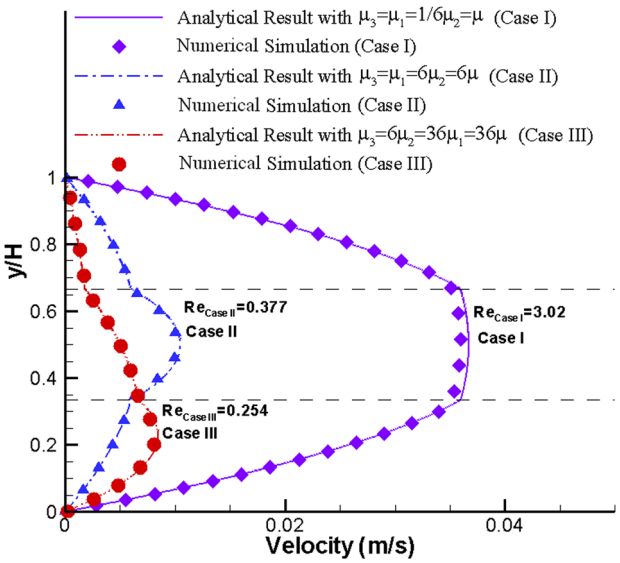


**Fig. 4 Three-layer pressure-driven flow**

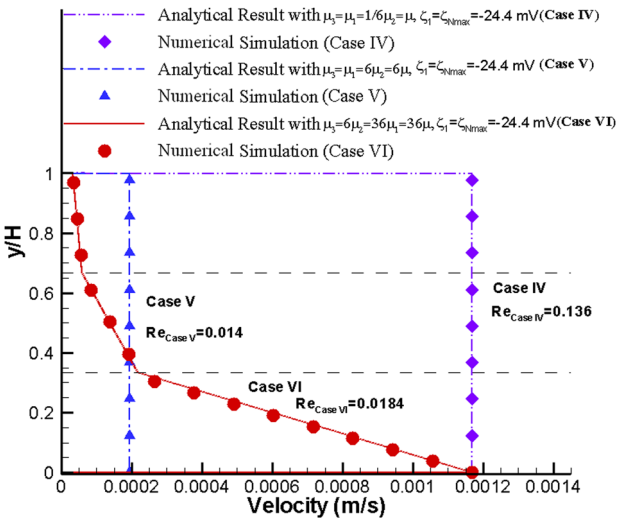


**Fig. 5 Three-layer electroosmotic flow with $\zeta_{Nmax} = \zeta_1 = -24.4mV$**

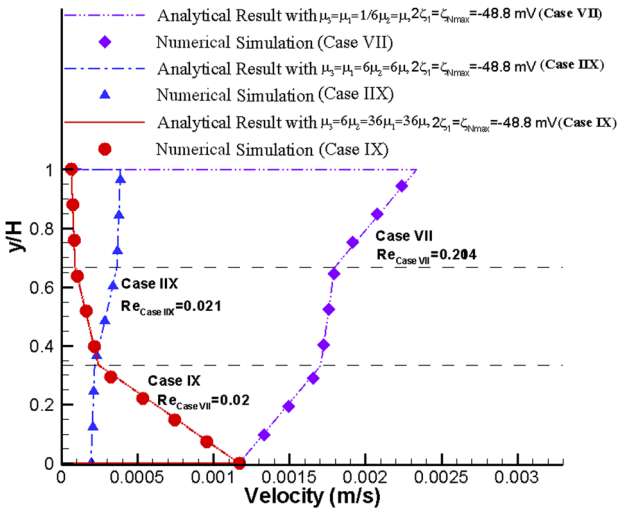


**Fig. 6 Three-layer electroosmotic flow with $\zeta_{\mathrm{Nmax}} = 2\zeta_1 = -48.8mV$**

constructed by adjusting the layers' heights and fluid viscosities for a given pressure drop. Figure 5 depicts the velocity profiles for three cases under electroosmotic flow condition. In Case IV the same top/bottom-wall $\zeta$ potentials, i.e.,− 24 mV, and low viscosities were enforced. The electrokinetic diffuse layer of thickness $\lambda_D$, which moves with electroosmotic velocity $u_{EO}$, generates a uniform velocity profile because all three fluid layers "ride" on that EDL. For Case V the same type of profile is achieved; however, at a much lower flow rate because the more viscous layers were placed along the channel walls. Clearly, maximum velocities can be generated when placing the most viscous fluid in the center and the least viscous ones on the solid surfaces. A stepwise profile appears when the viscosity increases from layer to layer (see Case VI). Compared to Figs. 5 and Fig. 6 demonstrates that various velocity profiles can be produced when applying different $\zeta$ potentials at the two walls (e.g., $\zeta_{\mathrm{Nmax}} = 2\zeta_1 = -48.8mV$). A larger $\zeta$ potential causes the wall fluid-layer to move faster and drag the bulk fluid along at a speed which depends on the assigned viscosities of the core layers. As a result, stepwise profiles appear for Cases VII – IX, characterized by their given viscosity distributions.

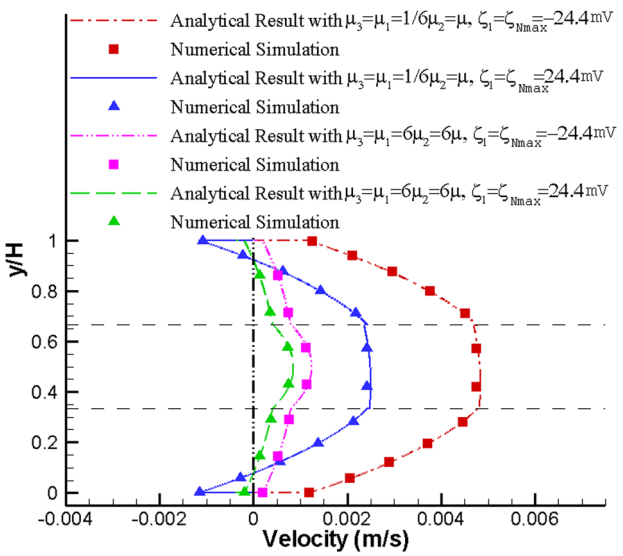


**Fig. 7 Three-layer combined electroosmotic and pressure-driven flow**

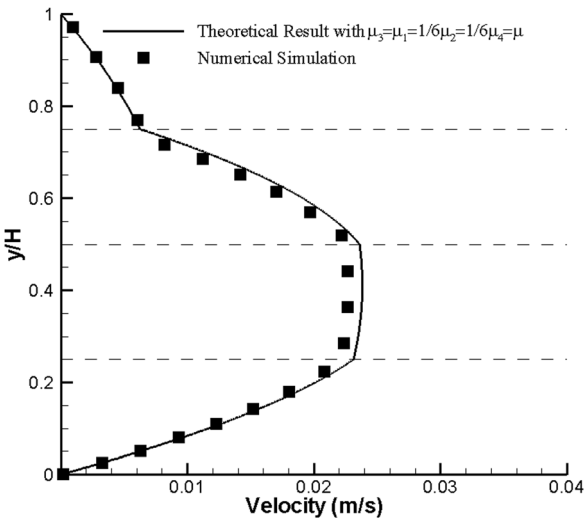


**Fig. 8 Four-layer pressure-driven flow**

If both pressure and electro-static forces are applied to microchannel flow, the resulting velocity profiles exhibit the combined effects. Specifically, Fig. 7 shows the profiles due to a pressure gradient plus electroosmosis (i.e., $\zeta_1 = \zeta_{\mathrm{N\,max}} = \pm 24.4mV$) with slip effects at both walls. For this case study, $\Delta p = 100Pa$ was used, instead of $\Delta p = 1000Pa$, in order to better contrast mechanical to electroosmotic flow. Clearly, the electroosmotic flow in the thin EDL layer is aiding the bulk flow when applying a positive electro-static force, while some backward flow may occur when using a negative Coulomb force. The impact of different EDL-thicknesses (i.e., actually $\lambda_D$-values) on velocity profiles is only apparent when the diffuse layer is in the micrometer range. In reality, the EDL-thickness is usually less than 100 nm. Thus, a slip velocity at the wall, in terms of electroosmotic velocity $u_{EO}$, can well describe the electroosmotic flow effect in pressure-driven microchannel flows.

**4.2 Four-Layer Flow.** To demonstrate the general applicability and accuracy of the analytical and computational models two 4-layer flow cases have been analyzed, considering pure pressure-driven flow (Fig. 8) and pure electroosmotic flow (Fig. 9). The viscosity distribution is $\mu_1 = \mu_3 = \mu, \mu_2 = \mu_4 = 6\mu$. For the electroosmotic flow, the top wall $\zeta$ potential is twice that of the bottom wall ($\zeta_{\mathrm{Nmax}} = 2\zeta_1 = -48.8mV$). As shown in Fig. 8, the highly viscous top fluid layer #4 causes a shifted

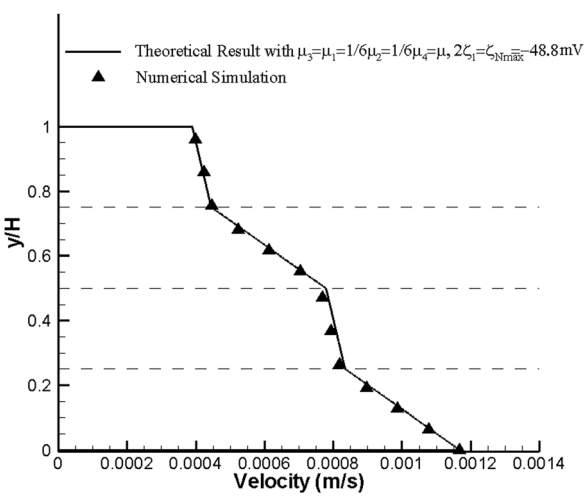


**Fig. 9 Four-layer electroosmotic flow**

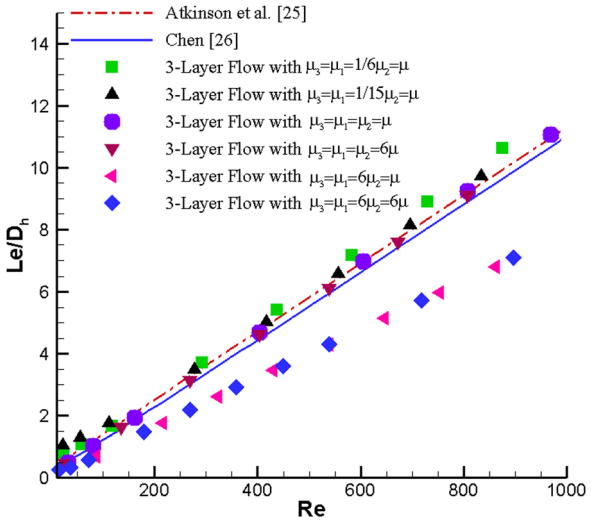


**Fig. 10 Entrance effect for three-layer pressure-driven flow**

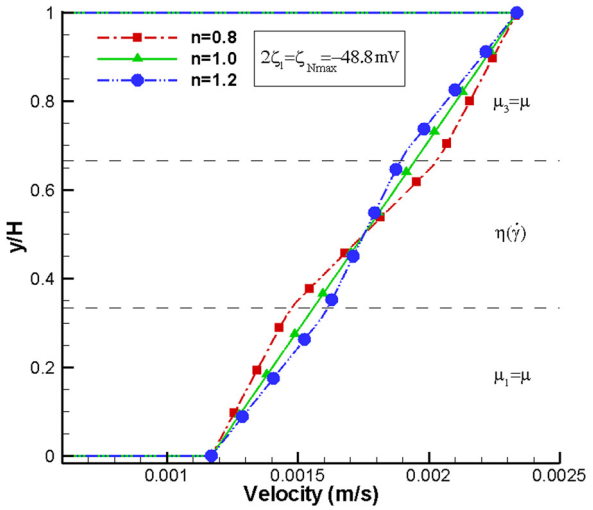


**Fig. 12 Three-layer electroosmotic flow with power-law fluid in the middle layer**

velocity profile which recovers symmetric features due to the low-viscosity layers # 1 and #3. In contrast, layered electroosmotic flows generate steplike velocity distributions (see Fig. 9). Again, the present model allows for the generation of desired/required velocity profiles in multilayer microchannel flow as a function of layered viscosity distribution and type of driving force.

**4.3 Entrance Effect.** In order to investigate the entrance effect of multilayer flow in microchannels, several three-layer flow simulation results were compared (see Fig. 10) to experimental correlations (i.e., Eqs. (7) and (8)) of Atkinson et al. [25] and Chen [26]. For symmetric viscosity distributions with the most viscous fluid-layer in the center, the simulation results for the dimensionless entrance length as a function of Reynolds number match the correlations quite well. Shorter entrance lengths appear when the centered fluid-layer is less viscous than the two fluid layers along the wall. The higher viscosities in the outer layer effectively decrease the velocity gradients, resulting in shorter entrance lengths. In comparison with experimental correlations for the one-layer parallel plate flow [25,26], the slope decreased from 0.011 to 0.008 (nearly 30%). For such cases, a simple correlation is proposed:

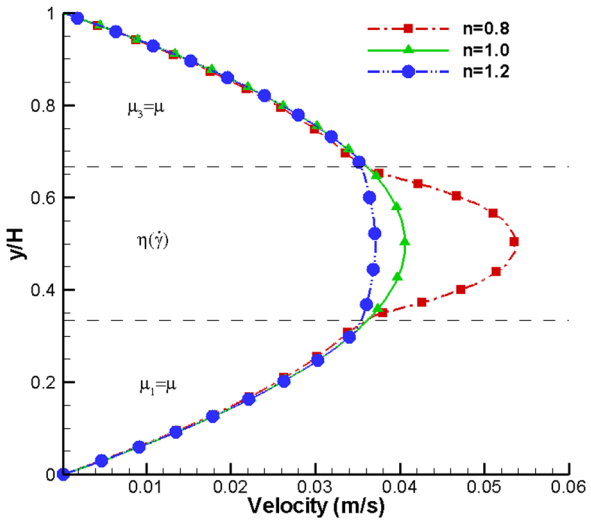


**Fig. 11 Three-layer pressure-driven flow with power-law fluid in the middle layer**

$$\frac{Le}{D_h} \approx 0.008\mathrm{Re} \tag{60}$$

Considering uniform inlet flow for three, evenly spaced layers, a computer experiment demonstrated that the middle layer thins out in the flow-developing region, regardless if it has a higher or lower viscosity compared to the equal viscosities of the fluid wall-layers. The reason is that the middle layer has always the largest average velocity and hence the center-layer thickness reduces in order to keep the same flow rate. For a particular case, e.g., $\mu_1 = \mu_3 = 6\mu_2 = 6\mu$, the middle layer may shrink about 30% within the entrance region.

**4.4 Power-Law Fluid Flow.** Biochemical multilayer flow applications may involve polymeric liquids described by the two-parameter power-law (see Eq. (4)). Hence, two cases of three-layer fluid flow with typical power-law fluids in the middle layer were investigated. As shown in Fig. 11, a pressure-driven layer of pseudoplastic fluid ($n < 1$) moves faster than its dilatational counterpart ($n > 1$), or the Newtonian fluid equivalent ($n = 1$). Considering pure electroosmotic power-law fluid flow subject to different wall $\zeta$ potentials, i.e., $\zeta_{\mathrm{Nmax}} = 2\zeta_1 = -48.8mV$, Fig. 12 depicts the resulting asymmetric velocity profiles for $n = 0.8$, 1.0, and 1.2. Obviously, the different $\zeta$ potentials induce a linear velocity distribution for $n = 1$ (Newtonian fluid), while nonlinear profiles are generated based on the given n-values characterizing the fluid. The centerline velocity is the same for all three cases because of the assumed constant inlet flow rate.

## 5 Conclusions

In this study, pressure-driven and/or electroosmotic immiscible multilayer flows in microchannels have been investigated. Assuming steady laminar fully-developed flow, general equations for velocity and shear stress profiles of $N$ layers of different viscosities were derived, resulting in a compact set of equations that can be used to explore various fluid properties and system parameters for any number of fluid layers. The numerical simulation results, using ANSYS CFX, match theoretical results, which can be readily programmed using analytical mathematics software such as MATLAB. Entrance flow effects with centered fluid-layer shrinking were studied as well. Specifically, cases with larger viscosities in the inner layers show a very good agreement with experimental correlations for the dimensionless entrance length as a function of inlet Reynolds number. However, significant deviations may occur for multilayer flows with smaller viscosities in the inner

layers. A correlation was deducted for the two-layer electroosmotic flow and the pressure driven flow, both being more complex when compared with single-layer flows. The impact of using power-law fluids on resulting velocity profiles has also been explored and compared to Newtonian fluid flows. The present model readily allows for an exploration of the impact of design choices on velocity profiles, shear stress, and channel distribution in multilayer microchannel flows as a function of layered viscosity distribution and type of driving force.

## Acknowledgment

The use of ANSYS-CFX12 (Ansys, Inc., Canonsburg, PA) is gratefully acknowledged. This study originated from a course project in "Microfluidics and Nanofluidics," MAE Department, NC State University, Raleigh, NC.

## References

[1] Ganan-Calvo, A. M., Gonzalez-Prieto, R., Riesco-Chueca, P., Herrada, M. A., and Flores-Mosquera, M., 2007, "Focusing Capillary Jets Close to the Continuum Limit," Nat. Phys., **3**(10), pp. 737–742.

[2] Okushima, S., Nisisako, T., Torri, T., and Higuchi, T., 2004, "Controlled Production of Monodisperse Double Emulsions by Two-Step Droplet Breakup in Microfluidic Devices," Langmuir, **20**(23), pp. 9905–9908.

[3] Ward, T., Faivre, M., Abkarian, M., and Stone, H. A., 2005, "Microfluidic Flow Focusing: Drop Size and Scaling in Pressure Versus Flow-Rate-Driven Pumping," Electrophoresis, **26**(19), pp. 3716–3724.

[4] Zheng, B., Tice, J. D., Roach, L. S., and Ismagilov, R. F., 2004, "A Droplet-Based, Composite PDMS/Glass Capillary Microfluidic System for Evaluating Protein Crystallization Conditions by Microbatch and Vapor-Diffusion Methods with On-Chip X-ray Diffraction," Angew. Chem., Int. Ed., **43**(19), pp. 2508–2511.

[5] Garstecki, P., Gitlin, I., Diluzio, W., Whitesides, G. M., Kumacheva, E., and Stone, H. A.,.2004, "Formation of Monodisperse Bubbles in a Microfluidic Flow-Focusing Device," Appl. Phys. Lett., **85**(13), pp. 2649–2651.

[6] Hettiarachchi, K., Lee, A. P., Zhang, S., Feingold, S., and Dayton, P.A., 2009, "Controllable Microfluidic Synthesis of Multiphase Drug-Carrying Lipospheres for Site-Targeted Therapy," Biotechnol. Prog., **25**(4), pp. 938–945.

[7] Chen, C. H., Shah, R. K., Abate, A. R., and Weitz, D. A., 2009, "Janus Particles Template from Double Emulsion Droplets Generated Using Microfluidics," Langmuir, **25**(8), pp. 4320–4323.

[8] Guillot, P., Moulin, T., Kotitz, R., Guirardel, M., Dodge, A., Joanicot, M., Colin, A., Bruneau, C. H., and Colin, T., 2008, "Towards a Continuous Microfluidic Rheometer," Microfluid. Nanofluid., **5**(5), pp. 619–630.

[9] Gunther, A., and Jensen, K. F., 2006, "Multiphase Microfluidic: From Flow Characteristics to Chemical and Materials Synthesis," Lab Chip, **6**(12), pp. 1487–1503.

[10] Kobayashi, J., Mori, Y., Okamoto, K., Akiyama, R., Ueno, M., Kitamori, T., and Kobayashi, S., 2004, "A Microfluidic Device for Conducting Gas-Liquid-Solid Hydrogenation Reactions," Science, **304**(5675), pp. 1305–1308.

[11] Maruyama, T., Matsushita, H., Uchida, J., Kubota, F., Kamiya, N., and Goto, M., 2004, "Liquid Membrane Operations in a Microfluidic Device for Selective Separation of Metal Ions," Anal. Chem., **76**(15), pp. 4495–4500.

[12] Maruyama, T., Uchida, J., Ohkawa, T., Futami, T., Katayama, K., Nishizawa, K., Sotowa, K., Kubota, F., Kamiyaa, N., and Goto, M., 2003, "Enzymatic Degradation of p-Chlorophenol in a Two-Phase Flow Microchannel System," Lab Chip, **3**(4), pp. 308–312.

[13] Surmerian, M., Slyadnev, M. N., Hisamoto, H., Hibara, A., Uchiyama, K., and Kitamori, T., 2002, "Three-Layer Flow Membrane System on a Microchip for Investigation of Molecular Transport," Anal. Chem., **74**(9), pp. 2014–2020.

[14] Zhao, B., Viernes, N. O. L., Moore, J. S., and Beebe, D. J. 2002, "Control and Applications of Immiscible Liquids in Microchannels," J. Am. Chem. Soc., **124**(19), pp. 5284–5285.

[15] Soohoo, J. R., and Walker, G. M., 2009, "Microfluidic Aqueous Two Phase System for Leukocyte Concentration from Whole Blood," Biomedical Microdevices, **11**(2), pp. 323–329.

[16] Wang, F., Wang, H., Wang, J., Wang, H. Y., Rummel, P. L., Garimella, S. V., and Lu, C., 2008, "Microfluidic Delivery to Small Molecules into Mammalian Cells Based on Hydrodynamic Focusing," Biotechnol. Bioeng., **100**(1), pp. 150–158.

[17] Takayama, S., Ostuni, E., LeDuc, P., Naruse, K., Ingber, D. E., and Whitesides, G. M., 2003, "Selective Chemical Treatment of Cellular Microdomains Using Multiple Laminar Streams," Chem. Biol., **10**(2), pp. 123–130.

[18] Kleinstreuer, C., 2010, *Modern Fluid Dynamics: Basic Theory and Selected Applications in Macro- and Micro-Devices* (Springer, Dordrecht, The Netherlands).

[19] Dutta, P., and Beskok, A., 2001, "Analytical Solution of Combined Electroosmotic/Pressure Driven Flows in Two-Dimensional Straight Channels: Finite Debye Layer Effects," Anal. Chem., **73**(9), pp. 1979–1986.

[20] Gao, Y., Wang, C., Wong, T. N., Nguyen, N. T., and Ooi, K.T., 2007, "Electro-Osmotic Control of the Interface Position of Two-Liquid Flow Through a Microchannel," Journal of Micromechanics and Microengineering, **17**, pp. 358–366.

[21] Gao, Y., Wong, T. N., Yang, C., and Ooi, K.T., 2005, "Two-Fluid Electroosmotic Flow in Microchannels," J. Colloid. Int. Sci., **284**, pp. 306–314.

[22] Li, H., Wong, T. N., and Nguyen, N-T., 2010, "Time –dependent Model of Mixed Electroosmotic/Pressure-Driven Three Immiscible Fluids in a Rectangular Microchannel," Int. J. Heat Mass Trans., **53**, pp. 772–785.

[23] Nguyen, N-T., and Wereley, S. T., 2006, *Fundamentals and Applications of Microfluidics* (Artech House, Boston, London).

[24] Kirby, B. J., 2010, Micro and Nanoscale Fluid Mechanics-Transport in Microfluidic Devices (Cambridge University, Cambridge).

[25] Arkinson, B., Brocklebank, M. P., Card, C. C., and Smith, J. M., 1969, "Low Reynolds Number Developing Flows," AIChE J., **15**(4), pp. 548–553.

[26] Chen, R.-Y., 1973, "Flow in the Entrance Region at Low Reynolds Numbers," ASME J. Fluids Eng., **95**, pp. 153–158.

[27] Gu, Y., and Li, D., 1997, "An Electrical Suspension Method for Measuring the Electric Charge on Small Silicon Oil Droplets Dispersed in Aqueous Solutions," J. Colloid Int. Sci., **195**, pp. 343–352.

[28] Gu, Y., and Li, D., 1998, "The $\zeta$-Potential of Silicone Oil Droplets Dispersed in Aqueous Solutions," J. Colloid Interface Sci., **206**, pp. 346–349.

[29] Li, H., Wong, T. N., and Nguyen, N-T., 2009, "Electroosmotic Control of Width and Position of Liquid Streams in Hydrodynamic Focusing," Microfluid. Nanofluid., **7**, pp. 489–497.